



Supplementary Materials for

**Group formation and cohesion of active particles with
visual perception–dependent motility**

François A. Lavergne, Hugo Wendehenne, Tobias Bäuerle, Clemens Bechinger*

*Corresponding author. Email: clemens.bechinger@uni-konstanz.de

Published 5 April 2019, *Science* **364**, 70 (2019)
DOI: 10.1126/science.aau5347

This PDF file includes:

Materials and Methods

Supplementary Text

Figs. S1 to S4

Captions for movies S1 to S5

References

Other supplementary material for this manuscript includes:

Movies S1 to S5

Materials and Methods

1 Experiments

1.1 Colloidal sample

We use spherical silica particles of diameter $\sigma = 4.28 \mu\text{m}$ coated with a 30 nm-thick carbon cap on one hemisphere, suspended in a critical mixture of water-lutidine at temperature $T = 26^\circ\text{C}$, which is several degrees below the demixing temperature $T_C = 34.1^\circ\text{C}$ (35). The particles are confined to the bottom plane of a 200 μm -thick sample cell (Hellma Analytics) by gravity. The glass cell is cleaned in an O_2 -plasma in order to render the surface negatively charged and avoid particles to stick to it. Under illumination, the carbon caps are heated above T_C , leading to a local demixing of the solvent near the caps (36). As a result of the compositional flows within the solvent, particles self-propel in the direction opposite to the orientation of the capped hemisphere (28, 36, 37). Due to hydrodynamics, the dynamics is restricted to two-dimensions (38). The translational diffusion coefficient has been determined from the mean-square displacement (39) to $D_0^{\text{exp}} = 0.023 \pm 0.003 \mu\text{m}^2/\text{s}$.

1.2 Experimental realization of individual tuning of the particle motility

To control the propulsion velocity of each particle independently, we take images of the particle configuration at a frequency of 2 Hz. The particle positions and orientations (which are defined as the vector from the capped side to the uncapped side of the particle (28)) are obtained by real time image analysis on a computer. This information is used to send a 532 nm laser beam (Laser Quan-

tum) to the determined centers with an acousto-optical deflector (AA Opto-electronic). Each particle is illuminated with a laser spot of width $5.5\text{ }\mu\text{m}$ for a period of $16\text{ }\mu\text{s}$ every 3 ms . Since the remixing timescale of the water-lutidine mixture is in the order of 100 ms (28, 35), the repetition is fast enough to produce steady self-propulsion conditions. Below an intensity of $I \approx 0.09\text{ W/mm}^2$, the velocity of the self-propelled particle is $v = 0\text{ }\mu\text{m/s}$, leading to Brownian diffusion of the particle. Above this threshold (and within the intensity range used in our work), the velocity v is proportional to the intensity of the illumination (Fig. S1(a)). It is important to notice that the reorientation of the particles is not affected by the laser illumination, and is still undergoing free rotational Brownian diffusion. Indeed, the rotational diffusion time (39, 40) remains constant at $\tau_R = 107 \pm 5\text{ s}$ (Fig. S1(b)).

Depending on their perception, the illumination intensity of each particle is set to either $I = 0.28\text{ W/mm}^2$ ($v_0 = 0.2\text{ }\mu\text{m/s}$, active particle) or to $I = 0\text{ W/mm}^2$ (passive particle). To avoid velocity changes due to the overlap of the illuminating Gaussian beams of neighboring particles, we have additionally adjusted the laser intensity depending on the relative particle positions (21). Particle configurations are updated every 500 ms . The typical displacement of a particle during this time interval is below 5% of the particle diameter, hence the feedback-loop can be considered as quasi-instantaneous.

Note that our system differs from other existing feedback systems (41, 42) because propulsion is achieved by self-diffusiophoresis and not by thermophoresis. This enables us to use much lower intensities (2 to 3 orders of magnitude lower) and thus to handle much higher numbers of particles (~ 100 as opposed to only a few), which is a key advantage to study collective phenomena.

1.3 System preparation

The experiment starts from a homogeneous distribution of N particles within a circular region of radius R_0 with empty surroundings. To achieve this, we use the fact that our particles respond to light intensity gradients (37). Namely, in a gradient of intensity, particles are subject to active torques that re-orient them towards the regions of lower intensities. Displacing the illuminating laser beam relative to the particle center by $\simeq 2.2 \mu\text{m}$ creates a local intensity gradient that “expells” the particles away from the center of the beam. Using this protocol for 10 min is usually sufficient to remove the particles outside of the circular region. The perception-motility rule starts after this period, corresponding to $t = 0$ s. A similar protocol using active torques is used at the edges of the field of view to create reflective boundary conditions, so that no particle enters the field of view during the entire measurement. The region of radius $R_0 = 106 \mu\text{m}$ contains on average $N = 75$ particles, corresponding to a density $\rho_0 = 2.1 \times 10^{-3} \mu\text{m}^2$.

1.4 Radius of gyration

For the cases where $P^* = P_\alpha^c$ and $\alpha \leq \pi/2$, we measured the density and the radial polarisation density profiles in the steady state. To define the steady state, we use the radius of gyration R_g of the particle distribution as an indicator of the size of the group. Figure S2 shows that R_g decreases as the particles gather in a small group. It then reaches a constant when the group is steady and cohesive, which we define as the steady state. The time τ_{ss} after which the group enters the steady state is obtained via an exponential fit of the form $R_g^{\text{fit}}(t) = A \exp(-t/B) + C$, and we take $\tau_{ss} = 4B$. Remarkably, even in the steady state, R_g can still be subject to high fluctuations as the groups can

undergo considerable particle reconfigurations.

1.5 Detection of aggregates

We consider that two particles belong to the same aggregate when they are separated by less than $l_p = 21.4 \mu\text{m}$, which corresponds to the persistence length. We then measure the time evolution of the mean size of aggregates. The latter reaches a constant value $\langle s \rangle$, which is reported in Fig. 3(b) of the main text. If $\langle s \rangle / N \lesssim 1$, particles form a single group and $\langle s \rangle / N \ll 1$ indicates the presence of multiple small aggregates.

1.6 Control of P^*/P_α^c

The control of P^*/P_α^c by variation of P^* can be problematic in experiments. In particular at low P^* , h is large and can be located outside our field of view, which does not allow to experimentally determine ϕ_h .

To solve this issue, we fix the threshold to $P^* = \alpha N / (\pi^2 R')$, where $R' = 106 \mu\text{m}$. The rescaled variable used in Fig. 4 of the main text is then

$$\frac{P^*}{P_\alpha^c} = \frac{\alpha N}{\pi^2 R'} \frac{\pi^2 R_0}{\alpha N} = \frac{R_0}{R'}, \quad (1)$$

which can be adjusted by varying R_0 at fixed R' . In the experiments we use $R_0 = 22.4, 42, 64.4$, and $106 \mu\text{m}$ ($P^* = P_\alpha^c$). In the far field approximation, $P^* \simeq N/(2\pi h)$ so

$$\frac{P^*}{P_\alpha^c} \simeq \frac{\pi}{2\alpha} \frac{R_0}{h}. \quad (2)$$

The case $R_0 = h$ then corresponds to the curve of equation $P^*/P_\alpha^c = \pi/(2\alpha)$, as shown in Fig. 4 of the main text.

2 Simulations

Simulations of active Brownian particles without volume exclusion are run by iterating the following discrete Langevin equations, for the position (x, y) and orientation $\hat{p} = (\cos \phi, \sin \phi)$ of each particle (43):

$$\begin{cases} x_{i,k} &= x_{i,k-1} + v(P_{i,k-1}) \cos \phi_{i,k-1} \Delta t + \sqrt{2D_0 \Delta t} \eta_{i,k}^{(x)} \\ y_{i,k} &= y_{i,k-1} + v(P_{i,k-1}) \sin \phi_{i,k-1} \Delta t + \sqrt{2D_0 \Delta t} \eta_{i,k}^{(y)} \\ \phi_{i,k} &= \phi_{i,k-1} + \sqrt{2D_R \Delta t} \eta_{i,k}^{(\phi)}, \end{cases} \quad (3)$$

where i is the particle index, k the step number, and Δt the value of the time increment. The terms $\eta^{(x)}$, $\eta^{(y)}$, and $\eta^{(\phi)}$ are three normally distributed random numbers with variance 1 and zero mean, and $P_{i,k-1} = \sum_{j \in V_\alpha^i} 1/(2\pi r_{ij})$ is the discrete perception of particle i at step $k-1$. The values of the translational and rotational diffusion coefficients are set consistent to the experimentally measured values, namely $D_0 = 0.02 \mu\text{m.s}^{-1}$ and $D_R = 1/110 \text{s}^{-1}$. The motility-response rule is a step function $v(P) = v_0 \Theta(P - P^*)$, with $v_0 = 0.2 \mu\text{m/s}$ as in the experiment. The time increment is set to $\Delta t = 0.5 \text{s}$, which corresponds to the update rate of the spot sequence in the experiment, leading to typical particle displacements smaller than of $\simeq 0.05\sigma$ between two iterations. The simulation is run for $N = 75$ particles, starting from a homogeneous circular distribution of radius $R_0 = 24\sigma$, for 10^5 steps, i.e. $5 \times 10^4 \text{s}$ of Brownian dynamics time. Movies S2 and S4 correspond to shorter simulations of 10^4 steps to fit the typical duration of an experiment. The vision cone angle and the perception threshold are varied in the range $\alpha \in [0; \pi]$ and $P^*/P_{\pi/2}^c \in [0; 2]$.

Supplementary text

3 Perception function

3.1 Discrete version

In a 2D system, the number of individuals located at a distance r from a given individual in the direction θ is given by $\delta N(r, \theta) = r \delta \theta \delta r \rho(r, \theta)$, where $r \delta \theta \delta r$ is an elementary area centred around the point (r, θ) , and $\rho(r, \theta)$ is the local number density of individuals. We define the average of $\rho(r, \theta)$ over all distances and angles accessible to the reference individual by

$$\bar{\rho} = \frac{1}{2\pi M} \int_0^M \int_0^{2\pi} \rho(r, \theta) d\theta dr, \quad (4)$$

where the distance varies from $r = 0$ to that of the furthest individual $r = M$, and angles are comprised between $\theta = 0$ and 2π . Using the Riemann integral

$$\int_0^M \int_0^{2\pi} \frac{\delta N(r, \theta)}{r \delta \theta \delta r} d\theta dr \simeq \sum_k \sum_l \frac{\Delta N(r_k, \theta_l)}{r_k},$$

one can rewrite $\bar{\rho}$ as

$$\bar{\rho} = \frac{1}{M} \sum_k \sum_l \frac{\Delta N(r_k, \theta_l)}{2\pi r_k}.$$

So far, the sum runs over bins (r_k, θ_l) containing $\Delta N(r_k, \theta_l)$ individuals each. Instead, summing over the individuals j perceived by an individual i gives

$$\bar{\rho}_i = \frac{1}{\max_{r_{ij}}} \sum_{j \neq i} \frac{1}{2\pi r_{ij}}, \quad (5)$$

where $r_{ij} = |\vec{r}_j - \vec{r}_i|$ is the distance between i and j , and $\max_{r_{ij}} = M$. We now define the perception of individual i as the average perceived density multiplied

by the perception range, $P_i = \max(r_{ij})\bar{\rho}_i$, which simply reads

$$P_i = \sum_{j \neq i} \frac{1}{2\pi r_{ij}}. \quad (6)$$

In the main text, we restrict the field of view to the vision cone V_i^α of an individual i with orientation \hat{p}_i , defined by

$$j \in V_i^\alpha \Leftrightarrow \hat{p}_i \cdot \frac{\vec{r}_j - \vec{r}_i}{|\vec{r}_j - \vec{r}_i|} \geq \cos \alpha. \quad (7)$$

Note that $i \notin V_i^\alpha$. In this case, the perception becomes

$$P_i = \sum_{j \in V_i^\alpha} \frac{1}{2\pi r_{ij}}. \quad (8)$$

The $\sim 1/r$ decay implies that the observer's perception due to a single individual at a distance r equals the perception due to N individuals at a distance $N \times r$. This invariance of the perception as long as the number of sources increases proportionally to the distance can be seen also from the far field expression $P_i \simeq N/(2\pi r)$, which is invariant under the change $N \rightarrow kN$ and $r \rightarrow kr$, where k is a constant. Note that due to the vision cone, the perception of one particle i is anisotropic when $\alpha < \pi$. As a consequence, the interaction between two particles i and j is thus non-reciprocal (22, 23, 44, 45), since $j \in V_i^\alpha$ does not imply $i \in V_j^\alpha$.

3.2 Continuous version

We now express the perception function in its continuous version. We first note that $P_i = P(\vec{r}_i)$, where \vec{r}_i is the position of individual i . Using $r_{ij} = |\vec{r}_j - \vec{r}_i|$, Eq. (8) reads

$$P(\vec{r}_i) = \sum_{j \in V_i^\alpha} \frac{1}{2\pi |\vec{r}_j - \vec{r}_i|},$$

We then transform the expression using the 2D Dirac distribution, $\delta^{(2)}(\vec{r})$, as

$$P(\vec{r}_i) = \sum_{j \in V_i^\alpha} \int_{\mathbb{R}^2} \frac{\delta^{(2)}(\vec{r}' - \vec{r}_j)}{2\pi|\vec{r}' - \vec{r}_i|} d^2\vec{r}' = \int_{V_i^\alpha} \sum_{j \neq i} \frac{\delta^{(2)}(\vec{r}' - \vec{r}_j)}{2\pi|\vec{r}' - \vec{r}_i|} d^2\vec{r}',$$

where the sum and integral have been swapped together with their respective domains to leave the overall quantity invariant. To go further, we use the microscopic expression of the number density, $\rho(\vec{r}) = \sum_j \delta^{(2)}(\vec{r} - \vec{r}_j)$, to obtain $\sum_{j \neq i} \delta^{(2)}(\vec{r} - \vec{r}_j) = \rho(\vec{r}) + \delta^{(2)}(\vec{r} - \vec{r}_i)$, and we insert it in the expression of $P(\vec{r}_i)$. The term $\delta^{(2)}(\vec{r} - \vec{r}_i)$ does not contribute to the integral since $i \notin V_i^\alpha$, so that in the end

$$P(\vec{r}_i) = \int_{V_i^\alpha} \frac{\rho(\vec{r}')}{2\pi|\vec{r}' - \vec{r}_i|} d^2\vec{r}'. \quad (9)$$

The perception function can actually be defined at any point position \vec{r} in the 2D plane with a given vision cone $V^\alpha(\vec{r})$ by

$$P(\vec{r}) = \int_{V^\alpha(\vec{r})} \frac{\rho(\vec{r}')}{2\pi|\vec{r}' - \vec{r}|} d^2\vec{r}'. \quad (10)$$

This expression can easily be generalised to 3D as

$$P_{3D}(\vec{r}) = \int_{V^\alpha(\vec{r})} \frac{\rho(\vec{r}')}{4\pi|\vec{r}' - \vec{r}|^2} d^3\vec{r}', \quad (11)$$

and note that the decay in $\sim 1/r^2$ is identical to that of the energy flux of sound waves in 3D space (5), supporting the applicability of such a long-range perception function in physical contexts.

3.3 Perception in the centre of a circular group

The initial configuration in our experiments and simulations consists of a circular group of radius R_0 and homogeneous density $\rho_0 = N/(\pi R_0^2)$. The perception in the centre of that group can be calculated by simple integration of

Eq. (10) (setting $\vec{r} = \vec{0}$ in the centre) as

$$P_\alpha^c = \int_{-\alpha}^{\alpha} \int_0^{R_0} \frac{\rho_0}{2\pi r'} r' dr' d\theta = \frac{\alpha}{\pi} \rho_0 R_0 = \frac{\alpha N}{\pi^2 R_0}. \quad (12)$$

3.4 Numerical calculation of the perception profile and response horizon

In order to determine the perception corresponding to a homogeneous circular group numerically, we generate $N = 785$ uniformly distributed points in a circle of radius $R = 100$ (arbitrary units). We consider a test particle with polar coordinates $\vec{r} = (r, \theta)$, where $\vec{r} = 0$ corresponds to the centre of the group. We choose its orientation vector to be $\hat{p} = -\vec{r}/r = -\hat{r}$, so that the particle points towards the centre of the group. Its vision cone is then denoted $V_{\text{in}}^\alpha(r, \theta)$. We calculate the perception pointing inwards at distance r from the centre by averaging Eq. (8) over θ at constant r

$$P^{\text{in}}(r) = \left\langle \sum_{j \in V_{\text{in}}^\alpha(r, \theta)} \frac{1}{2\pi |\vec{r}_j - \vec{r}|} \right\rangle_{\theta \in [0; 2\pi]}. \quad (13)$$

and averaging over 10 different configurations. The perception profile is made dimensionless by computing $\tilde{P}^{\text{in}}(\tilde{r})$, where $\tilde{P}^{\text{in}} = P^{\text{in}}/P_\alpha^c$ (using $P_\alpha^c = \alpha N/(\pi^2 R)$), and $\tilde{r} = r/R$. The same calculations are performed for P^{out} (where $\hat{p} = +\hat{r}$) and P^{iso} (where $\alpha = \pi$). We checked that \tilde{P} versus \tilde{r} does not depend on N and R as long as the statistics is good enough.

For each experiment or simulation run, the perception profile P^{in} is obtained by $P^{\text{in}} = \tilde{P}^{\text{in}} P_\alpha^c$, where $P_\alpha^c = \alpha N/(\pi^2 R_0)$ and distances by $r = \tilde{r} R_0$, where R_0 is the radius of the corresponding initial state. The response horizon h is then obtained from $P^{\text{in}}(h) = P^*$ (the intersection of the profile and the threshold value).

3.5 Approximate expression and density perturbation

Here, we derive an approximate expression of the perception to first order in density gradients and for narrow vision cones. We change the variable in the integral of Eq. (10) to $\vec{u} = \vec{r}' - \vec{r}$ (the position in the co-moving frame of a particle located at \vec{r}) and obtain

$$P(\vec{r}) = \frac{1}{2\pi} \int_{-\alpha}^{\alpha} \int_0^L \rho(\vec{r} + \vec{u}) du d\theta,$$

where θ is such that $\vec{u} = u(\cos \theta \hat{p} + \sin \theta \hat{p}^\perp)$, and $L = \max(u)$ is the distance to the furthest perceived individual. In the limit $\alpha \rightarrow 0$ (highly non-reciprocal interactions (22, 23, 44, 45)), one has $\vec{u} \simeq u\hat{p}$ to the lowest order, which leads to

$$P(\vec{r}) = \frac{\alpha}{\pi} \int_0^L \rho(\vec{r} + u\hat{p}) du. \quad (14)$$

At short distances, $\rho(\vec{r} + u\hat{p}) \simeq \rho(\vec{r}) + u\hat{p} \cdot \vec{\nabla} \rho|_{u=0}$, and integration gives

$$P(\rho) = \frac{\alpha}{\pi} \rho L + \frac{\alpha L^2}{2\pi} \hat{p} \cdot \vec{\nabla} \rho, \quad (15)$$

where P is now seen as a function of ρ . A density perturbation $\delta\rho$ of a homogeneous state at ρ_0 leads to a variation of perception given by

$$\delta P = P(\rho_0 + \delta\rho) - P(\rho_0) = \frac{\alpha}{\pi} \delta\rho L + \frac{\alpha L^2}{2\pi} \hat{p} \cdot \vec{\nabla} \delta\rho. \quad (16)$$

4 Instability analysis

4.1 Density-dependent motility

The steady-state density distribution of active particles with a spatially-varying velocity is given by $\rho(\vec{r}) = c/v(\vec{r})$, where c is a constant. This means that

dilute (resp. dense) regions correspond to fast (resp. slow) particles (15). We now briefly remind the case of a velocity that *decreases* as a function of the *local* density of particles, i.e. $v = v(\rho)$ and $v'(\rho) < 0$, due to chemical signalling or repulsive interactions between the particles as discussed in (15). A perturbation $\delta\rho(\vec{r})$ of an initially homogeneous distribution of particles, $\rho_0 = cv(\rho_0)$, leads to a non-uniform velocity $v(\rho_0 + \delta\rho(\vec{r})) \simeq v(\rho_0) + v'(\rho_0)\delta\rho(\vec{r})$. The new steady state density is then

$$\rho_0 + \delta\rho' = \frac{c}{v(\rho_0) + v'(\rho_0)\delta\rho} = \frac{c}{v(\rho_0)(1 + \frac{v'(\rho_0)}{v(\rho_0)}\delta\rho)} \simeq \rho_0(1 - \frac{v'(\rho_0)}{v(\rho_0)}\delta\rho). \quad (17)$$

The perturbation grows if $\delta\rho' > \delta\rho$, i.e. if the following condition is met

$$v'(\rho_0) < -\frac{v(\rho_0)}{\rho_0}. \quad (18)$$

Thus, if the decay of the density-dependent velocity is "strong enough", the uniform state is linearly unstable to density perturbations. This is the basic mechanism of a motility-induced phase separation between a dilute gas and a dense cluster phase in absence of attractive interactions, as rigorously described in (15). However, the dense phase is not cohesive in this case since it exchanges particles with the co-existing gas.

4.2 Perception-dependent motility

We now show that the observation of cohesive group formation in our experiments and simulations can be understood as a motility-induced phenomenon. We consider that the velocity is an *increasing* function of a *long range* and *anisotropic* perception P , i.e. $v = v(P)$ with $v'(P) > 0$. This is very different from the aforementioned case but we apply the same treatment to work out an instability criterion in the following.

Under a density perturbation $\rho_0 \rightarrow \rho_0 + \delta\rho$, the perception of a particle changes as $P_0 \rightarrow P_0 + \delta P$, where $P_0 = P(\rho_0) = (\alpha/\pi)\rho_0 L$. In the limit $\alpha \rightarrow 0$ of high non-reciprocity, δP can be expressed from Eq. (16)

$$\delta P = P_0 \left(\frac{\delta\rho}{\rho_0} + \frac{L}{2\rho_0} \hat{p} \cdot \vec{\nabla} \delta\rho \right). \quad (19)$$

The new velocity then reads

$$\begin{aligned} v(P_0 + \delta P) &\simeq v(P_0) + v'(P_0)\delta P, \\ &\simeq v(P_0) \left(1 + \frac{v'(P_0)}{v(P_0)} P_0 \left(\frac{\delta\rho}{\rho_0} + \frac{L}{2\rho_0} \hat{p} \cdot \vec{\nabla} \delta\rho \right) \right). \end{aligned} \quad (20)$$

The steady state density $\rho_0 = c/v(P_0)$ changes as

$$\begin{aligned} \rho_0 + \delta\rho' &= \frac{c}{v(P_0 + \delta P)} \\ &= \frac{\rho_0}{1 + \frac{v'(P_0)}{v(P_0)} P_0 \left(\frac{\delta\rho}{\rho_0} + \frac{L}{2\rho_0} \hat{p} \cdot \vec{\nabla} \delta\rho \right)} \\ &\simeq \rho_0 \left(1 - \frac{v'(P_0)}{v(P_0)} P_0 \left(\frac{\delta\rho}{\rho_0} + \frac{L}{2\rho_0} \hat{p} \cdot \vec{\nabla} \delta\rho \right) \right) \\ &\simeq \rho_0 - \frac{v'(P_0)}{v(P_0)} P_0 \left(\delta\rho + \frac{L}{2} \hat{p} \cdot \vec{\nabla} \delta\rho \right). \end{aligned} \quad (21)$$

The perturbation increases if $\delta\rho' > \delta\rho$, leading to the condition

$$\frac{\hat{p} \cdot \vec{\nabla} \delta\rho}{\delta\rho} < -\frac{2}{L} \left(1 + \frac{v(P_0)}{v'(P_0)P_0} \right). \quad (22)$$

Since $v'(P_0)$ is positive, the right-hand side is always negative. As a consequence, the particles tend to accumulate where they are typically oriented opposite to density gradients (the density increases if $\hat{p} \cdot \vec{\nabla} \delta\rho / \delta\rho \ll 0$). Conversely, the perturbation always decreases when $\hat{p} \cdot \vec{\nabla} \delta\rho / \delta\rho > 0$. This means that particles aligned with density gradients *always* move away from these regions, where the density decreases until they are free from particles. The fact

that the instability depends on the relative orientation between the particles and density gradients leads a perturbation to develop asymmetrically as shown in Fig. S3, and eventually to the contraction of the initial configuration used in the experiments/simulations. This provides a purely kinetic mechanism of group formation, without requiring active reorientations.

5 Insertion of a blind zone

5.1 Definition

We also studied the case illustrated in Fig. S4(a), where a blind zone of half width β is inserted between the two halves of the vision cone, each of width α . The vision field of an individual i , denoted $V_i^{\alpha,\beta}$, is then defined by

$$j \in V_i^{\alpha,\beta} \Leftrightarrow \cos \beta \geq \hat{p}_i \cdot \frac{\vec{r}_j - \vec{r}_i}{|\vec{r}_j - \vec{r}_i|} \geq \cos(\alpha + \beta). \quad (23)$$

The perception in the centre P_α^c remains unchanged compared to the case of a single vision cone of half width α (case $\beta = 0$), and is independent of β .

5.2 Results

As an example, we discuss the data of experiments at fixed $\alpha = \pi/4$ corresponding to two different values of β . We fix the threshold to $P^* = 0.21P_\alpha^c$ by using $R_0 = 22.4\mu\text{m}$ and $R' = 106\mu\text{m}$ as explained in section 1.6.

Frontal vision: For $\beta = \pi/8$, the two halves of the vision cone point to the front of the particle, which is referred to as “frontal vision”. In this case, we observe in Fig. S4(b) that the final state is a cohesive group, similar to those obtained in zone I of the vision-threshold diagram (Fig. 4 of the main text) for $\beta = 0$.

Lateral vision: For $\beta = 3\pi/8$, the two halves of the vision cone are located on each side of the particle, and the blind zones at the front and rear of the particle are identical. In this case, referred to as “lateral vision”, no cohesive group is observed. Indeed, the initial group spreads and virtually all particles become passive by the end of the experiment, as shown in Fig. S4(b). This is similar to case III of the vision-threshold diagram (Fig. 4 of the main text) for $\beta = 0$.

5.3 Interpretation

In the case of frontal vision, the perception profile has the same features as those of Fig. 1(c) of the main text ($\alpha = \pi/4$, and $\beta = 0$). Namely, $P^{\text{in}} \neq P^{\text{out}}$ and P^{in} has a maximum as shown in Fig. S4(c). These features guarantee the activation of particles looking towards the group, so the cohesion mechanism is at work. Conversely, Fig. S4(c) shows that for lateral vision, the perception is the same for inwards and outwards pointing particles, and decays monotonically from the centre. This is similar to the case of an isotropic perception shown in Fig. 1(c) of the main text. Thus, the cohesion mechanism based on the difference between P^{in} and P^{out} is inexistant, so the particles spread until becoming passive.

These results show that a front-rear asymmetry in vision is essential for cohesion, be it present as a single vision cone or two halves of vision cone with a narrow blind zone in between. Indeed, this ensures $P^{\text{in}} \neq P^{\text{out}}$ and that the direction of perception and motion are aligned. However, when the vision has a front-rear symmetry, such as in the isotropic case or with two lateral halves of vision cone, one has $P^{\text{in}} = P^{\text{out}}$ and the direction of perception and motion are not aligned anymore, which leads to a loss of cohesion.

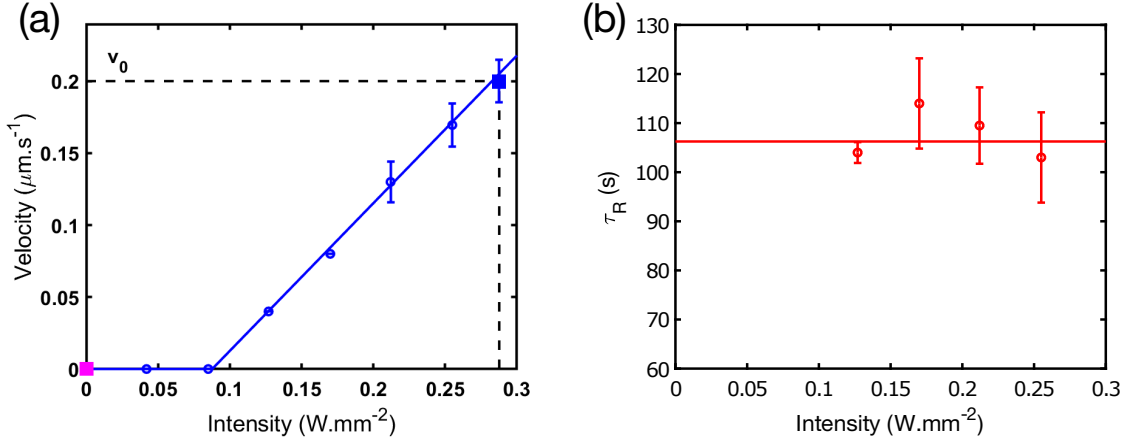


Fig. S1.: Control of particle dynamics as a function of the laser intensity. (a) Experimentally measured propulsion velocities (open symbols) obtained from the mean square displacement (39) depending on the laser illumination. In our experiment, we use $I = 0.28 \text{ W/mm}^2$ for active particles resulting in $v_0 = 0.2 \text{ }\mu\text{m/s}$ (blue square), and no illumination for passive particles (magenta square). Error bars correspond to the standard deviation on different measurements. (b) Experimentally measured rotational diffusion time obtained from the autocorrelation function of the particle orientation (open symbols) and theoretical one obtained from the Stokes-Einstein expression at infinite dilution ($\tau_R^{\text{theor}} = 106\text{s}$, horizontal line). The value of τ_R is extracted from the exponential decay of the autocorrelation function $\langle \cos \phi \rangle = \exp(-t/\tau_R)$, where $\hat{p} = (\cos \phi, \sin \phi)$ is the orientation vector of a particle (40). Importantly, the measured τ_R is not affected by the laser intensity, showing that the reorientation of the particles is undergoing rotational diffusion upon illumination. In this work, we use the averaged value of the measurements $\tau_R = 107 \pm 5\text{s}$.

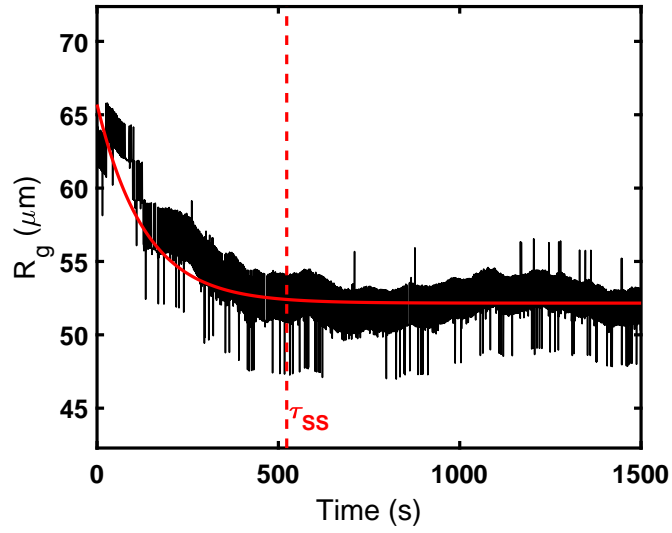


Fig. S2.: Time evolution of the radius of gyration of the group. Experimentally measured radius of gyration R_g (black line). The steady state is reached at τ_{SS} , as obtained from an exponential fit (red dashed line), after which R_g becomes constant. Parameters are set to $P^* = P_\alpha^c$ and $\alpha = \pi/12$.

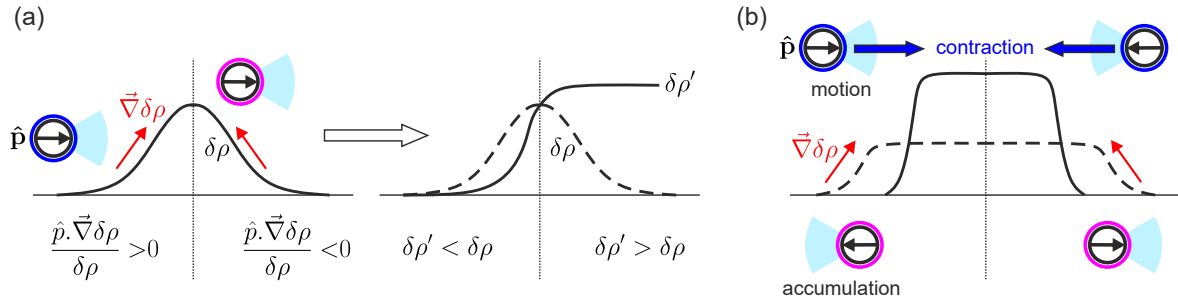


Fig. S3.: Evolution of a density perturbation. (a) The instability criterion in Eq. (22) implies that a density perturbation develops asymmetrically for a fixed particle orientation. We use a simplified criterion, $\delta\rho' > \delta\rho$ when $\hat{p} \cdot \vec{\nabla} \delta\rho / \delta\rho < 0$, which is true in the limit of large L . The particles have been colored according to their activity in the case of a threshold velocity-response to illustrate the behavior described in the main text, but the phenomenon happens in general for any $v(P)$ with $v'(P) > 0$. (b) Schematic representation of the evolution of the initial configuration used in the experiments/simulations. The group contracts under a flux imbalance: particles move along the concentration gradients but accumulate when going down the gradient, which prevents them from leaving.

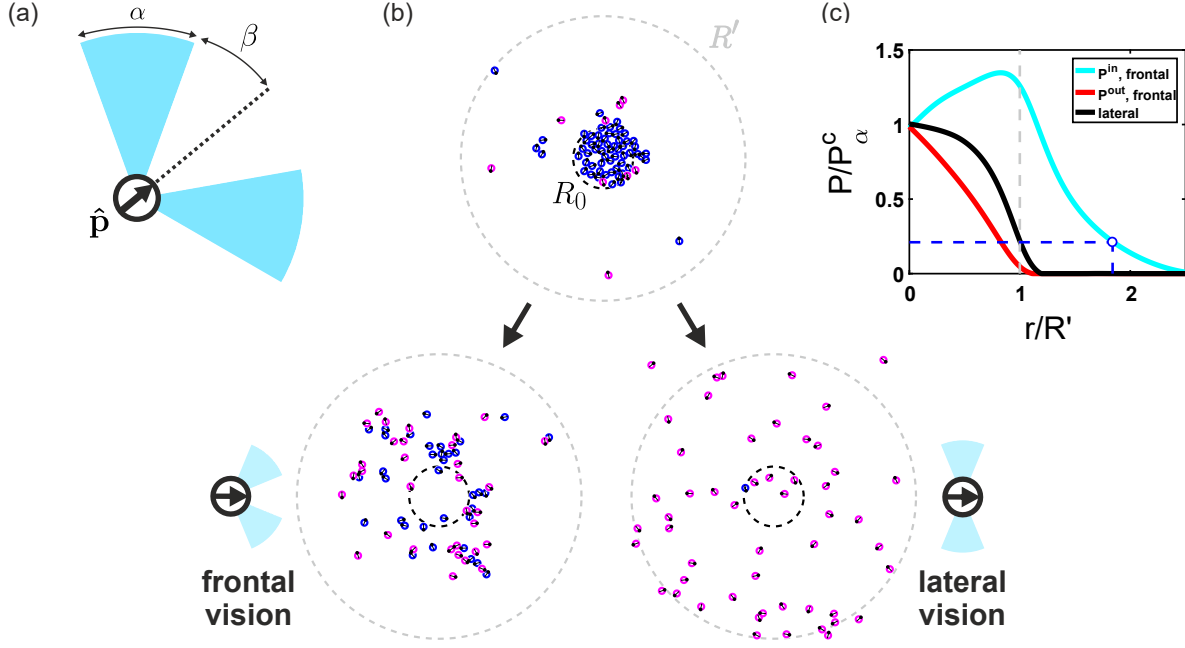


Fig. S4.: Group cohesion with a blind zone. (a) Definition of the blind zone of half width β , inserted between the two halves of the vision cone of width α each. (b) Initial (top) and final (bottom) experimental snapshots at fixed $\alpha = \pi/4$ for two different cases: $\beta = \pi/8$ (frontal vision, left), and $\beta = 3\pi/8$ (lateral vision, right). The threshold is set to $P^* = 0.21P_\alpha^c$ using the method in section 1.6 with $R_0 = 22.4\mu\text{m}$ and $R' = 106\mu\text{m}$. The final state is a cohesive group for frontal vision with a mixture of active (blue) and passive particles (magenta). For lateral vision, cohesion is absent as virtually all particles become passive. (c) Perception profiles in the case of frontal vision, for particles pointing inwards (cyan) and outwards (red). For lateral vision, the perception is independent of the inwards/outwards direction (black) due to the rear-back symmetry. The perception threshold at $0.21P_\alpha^c$ and the corresponding response horizon at $\simeq 1.8R'$ are shown by the blue dashed line for frontal vision.

Movie S1.

Group formation and cohesion in the case $v_0 = 0.2\mu\text{m/s}$, $\alpha = \pi/4$ and $P = P_\alpha^c$. The playback speed is $300\times$ faster than reality.

Movie S2.

Simulation of ideal particles (no volume exclusion, 10^4 time steps) with the same parameters as Movie S1. The playback speed is $300\times$ faster than the Brownian dynamics time.

Movie S3.

Group formation and cohesion in the case $v_0 = 0.2\mu\text{m/s}$, $\alpha = \pi/12$ and $P = P_\alpha^c$. The shape of the group is more elongated due to the high anisotropy of the very narrow vision cone. The playback speed is the same as Movie S1.

Movie S4.

Simulation of ideal particles (no volume exclusion, 10^4 time steps) with the same parameters as Movie S3. The playback speed is the same as Movie S2.

Movie S5.

Long time simulation of ideal particles (no volume exclusion, 10^5 time steps) with the same parameters as Movie S3. The playback speed is $10\times$ that of Movie S2.

References

1. M. Ballerini, N. Cabibbo, R. Candelier, A. Cavagna, E. Cisbani, I. Giardina, V. Lecomte, A. Orlandi, G. Parisi, A. Procaccini, M. Viale, V. Zdravkovic, Interaction ruling animal collective behavior depends on topological rather than metric distance: Evidence from a field study. *Proc. Natl. Acad. Sci. U.S.A.* **105**, 1232–1237 (2008). [doi:10.1073/pnas.0711437105](https://doi.org/10.1073/pnas.0711437105) [Medline](#)
2. A. Berdahl, C. J. Torney, C. C. Ioannou, J. J. Faria, I. D. Couzin, Emergent sensing of complex environments by mobile animal groups. *Science* **339**, 574–576 (2013). [doi:10.1126/science.1225883](https://doi.org/10.1126/science.1225883) [Medline](#)
3. J. L. Silverberg, M. Bierbaum, J. P. Sethna, I. Cohen, Collective motion of humans in mosh and circle pits at heavy metal concerts. *Phys. Rev. Lett.* **110**, 228701 (2013). [doi:10.1103/PhysRevLett.110.228701](https://doi.org/10.1103/PhysRevLett.110.228701) [Medline](#)
4. D. J. G. Pearce, A. M. Miller, G. Rowlands, M. S. Turner, Role of projection in the control of bird flocks. *Proc. Natl. Acad. Sci. U.S.A.* **111**, 10422–10426 (2014). [doi:10.1073/pnas.1402202111](https://doi.org/10.1073/pnas.1402202111) [Medline](#)
5. D. Gorbonos, R. Iancu, J. G. Puckett, R. Ni, N. T. Ouellette, N. S. Gov, Long-range acoustic interactions in insect swarms: An adaptive gravity model. *New J. Phys.* **18**, 073042 (2016). [doi:10.1088/1367-2630/18/7/073042](https://doi.org/10.1088/1367-2630/18/7/073042)
6. R. R. Kay, P. Langridge, D. Traynor, O. Hoeller, Changing directions in the study of chemotaxis. *Nat. Rev. Mol. Cell Biol.* **9**, 455–463 (2008). [doi:10.1038/nrm2419](https://doi.org/10.1038/nrm2419) [Medline](#)
7. I. D. Couzin, J. Krause, R. James, G. D. Ruxton, N. R. Franks, Collective memory and spatial sorting in animal groups. *J. Theor. Biol.* **218**, 1–11 (2002). [doi:10.1006/jtbi.2002.3065](https://doi.org/10.1006/jtbi.2002.3065) [Medline](#)
8. K. Tunstrøm, Y. Katz, C. C. Ioannou, C. Huepe, M. J. Lutz, I. D. Couzin, Collective states, multistability and transitional behavior in schooling fish. *PLOS Comput. Biol.* **9**, e1002915 (2013). [doi:10.1371/journal.pcbi.1002915](https://doi.org/10.1371/journal.pcbi.1002915) [Medline](#)
9. A. Cavagna, I. Giardina, Bird Flocks as Condensed Matter. *Annu. Rev. Condens. Matter Phys.* **5**, 183–207 (2014). [doi:10.1146/annurev-conmatphys-031113-133834](https://doi.org/10.1146/annurev-conmatphys-031113-133834)
10. P. Romanczuk, M. Bär, W. Ebeling, B. Lindner, L. Schimansky-Geier, Active Brownian particles. *Eur. Phys. J. Spec. Top.* **202**, 1–162 (2012). [doi:10.1140/epjst/e2012-01529-y](https://doi.org/10.1140/epjst/e2012-01529-y)
11. I. Theurkauff, C. Cottin-Bizonne, J. Palacci, C. Ybert, L. Bocquet, Dynamic clustering in active colloidal suspensions with chemical signaling. *Phys. Rev. Lett.* **108**, 268303 (2012). [doi:10.1103/PhysRevLett.108.268303](https://doi.org/10.1103/PhysRevLett.108.268303) [Medline](#)
12. J. Palacci, S. Sacanna, A. P. Steinberg, D. J. Pine, P. M. Chaikin, Living crystals of light-activated colloidal surfers. *Science* **339**, 936–940 (2013). [doi:10.1126/science.1230020](https://doi.org/10.1126/science.1230020) [Medline](#)

13. F. Ginot, I. Theurkauff, F. Detcheverry, C. Ybert, C. Cottin-Bizonne, Aggregation-fragmentation and individual dynamics of active clusters. *Nat. Commun.* **9**, 696 (2018). [doi:10.1038/s41467-017-02625-7](https://doi.org/10.1038/s41467-017-02625-7) [Medline](#)
14. I. Buttinoni, J. Bialké, F. Kümmel, H. Löwen, C. Bechinger, T. Speck, Dynamical clustering and phase separation in suspensions of self-propelled colloidal particles. *Phys. Rev. Lett.* **110**, 238301 (2013). [doi:10.1103/PhysRevLett.110.238301](https://doi.org/10.1103/PhysRevLett.110.238301) [Medline](#)
15. M. E. Cates, J. Tailleur, Motility-Induced Phase Separation. *Annu. Rev. Condens. Matter Phys.* **6**, 219–244 (2015). [doi:10.1146/annurev-conmatphys-031214-014710](https://doi.org/10.1146/annurev-conmatphys-031214-014710)
16. T. Vicsek, A. Czirók, E. Ben-Jacob, I. Cohen, O. Shochet, Novel type of phase transition in a system of self-driven particles. *Phys. Rev. Lett.* **75**, 1226–1229 (1995). [doi:10.1103/PhysRevLett.75.1226](https://doi.org/10.1103/PhysRevLett.75.1226) [Medline](#)
17. A. Bricard, J.-B. Caussin, N. Desreumaux, O. Dauchot, D. Bartolo, Emergence of macroscopic directed motion in populations of motile colloids. *Nature* **503**, 95–98 (2013). [doi:10.1038/nature12673](https://doi.org/10.1038/nature12673) [Medline](#)
18. G. Grégoire, H. Chaté, Onset of collective and cohesive motion. *Phys. Rev. Lett.* **92**, 025702 (2004). [doi:10.1103/PhysRevLett.92.025702](https://doi.org/10.1103/PhysRevLett.92.025702) [Medline](#)
19. D. J. G. Pearce, M. S. Turner, Density regulation in strictly metric-free swarms. *New J. Phys.* **16**, 082002 (2014). [doi:10.1088/1367-2630/16/8/082002](https://doi.org/10.1088/1367-2630/16/8/082002)
20. R. van Drongelen, A. Pal, C. P. Goodrich, T. Idema, Collective dynamics of soft active particles. *Phys. Rev. E* **91**, 032706 (2015). [doi:10.1103/PhysRevE.91.032706](https://doi.org/10.1103/PhysRevE.91.032706) [Medline](#)
21. T. Bäuerle, A. Fischer, T. Speck, C. Bechinger, Self-organization of active particles by quorum sensing rules. *Nat. Commun.* **9**, 3232 (2018). [doi:10.1038/s41467-018-05675-7](https://doi.org/10.1038/s41467-018-05675-7) [Medline](#)
22. L. Barberis, F. Peruani, Large-Scale Patterns in a Minimal Cognitive Flocking Model: Incidental Leaders, Nematic Patterns, and Aggregates. *Phys. Rev. Lett.* **117**, 248001 (2016). [doi:10.1103/PhysRevLett.117.248001](https://doi.org/10.1103/PhysRevLett.117.248001) [Medline](#)
23. M. Durve, A. Saha, A. Sayeed, Active particle condensation by non-reciprocal and time-delayed interactions. *Eur. Phys. J. E* **41**, 49 (2018). [doi:10.1140/epje/i2018-11653-4](https://doi.org/10.1140/epje/i2018-11653-4) [Medline](#)
24. A. Attanasi, A. Cavagna, L. Del Castello, I. Giardina, S. Melillo, L. Parisi, O. Pohl, B. Rossaro, E. Shen, E. Silvestri, M. Viale, Collective behaviour without collective order in wild swarms of midges. *PLOS Comput. Biol.* **10**, e1003697 (2014). [doi:10.1371/journal.pcbi.1003697](https://doi.org/10.1371/journal.pcbi.1003697) [Medline](#)
25. See supplementary materials.
26. J. R. Howse, R. A. L. Jones, A. J. Ryan, T. Gough, R. Vafabakhsh, R. Golestanian, Self-motile colloidal particles: From directed propulsion to random walk. *Phys. Rev. Lett.* **99**, 048102 (2007). [doi:10.1103/PhysRevLett.99.048102](https://doi.org/10.1103/PhysRevLett.99.048102) [Medline](#)

27. J. J. Gibson, Visually controlled locomotion and visual orientation in animals. *Br. J. Psychol.* **49**, 182–194 (1958). [doi:10.1111/j.2044-8295.1958.tb00656.x](https://doi.org/10.1111/j.2044-8295.1958.tb00656.x) [Medline](#)
28. J. R. Gomez-Solano, S. Samin, C. Lozano, P. Ruedas-Batuecas, R. van Roij, C. Bechinger, Tuning the motility and directionality of self-propelled colloids. *Sci. Rep.* **7**, 14891 (2017). [doi:10.1038/s41598-017-14126-0](https://doi.org/10.1038/s41598-017-14126-0) [Medline](#)
29. A. Cavagna, D. Conti, C. Cretto, L. Del Castello, I. Giardina, T. S. Grigera, S. Melillo, L. Parisi, M. Viale, Dynamic scaling in natural swarms. *Nat. Phys.* **13**, 914–918 (2017). [doi:10.1038/nphys4153](https://doi.org/10.1038/nphys4153)
30. D. H. Kelley, N. T. Ouellette, Emergent dynamics of laboratory insect swarms. *Sci. Rep.* **3**, 1073 (2013). [doi:10.1038/srep01073](https://doi.org/10.1038/srep01073) [Medline](#)
31. M. S. Banks, W. W. Sprague, J. Schmoll, J. A. Q. Parnell, G. D. Love, Why do animal eyes have pupils of different shapes? *Sci. Adv.* **1**, e1500391 (2015). [doi:10.1126/sciadv.1500391](https://doi.org/10.1126/sciadv.1500391) [Medline](#)
32. I. Slavkov, D. Carrillo-Zapata, N. Carranza, X. Diego, F. Jansson, J. Kaandorp, S. Hauert, J. Sharpe, Morphogenesis in robot swarms. *Sci. Robot.* **3**, eaau9178 (2018). [doi:10.1126/scirobotics.aau9178](https://doi.org/10.1126/scirobotics.aau9178)
33. L. Bayındır, A review of swarm robotics tasks. *Neurocomputing* **172**, 292–321 (2016). [doi:10.1016/j.neucom.2015.05.116](https://doi.org/10.1016/j.neucom.2015.05.116)
34. J.-L. Deneubourg, J.-C. Grégoire, E. Le Fort, Kinetics of larval gregarious behavior in the bark beetle *Dendroctonus micans* (Coleoptera: Scolytidae). *J. Insect Behav.* **3**, 169–182 (1990). [doi:10.1007/BF01417910](https://doi.org/10.1007/BF01417910)
35. J. C. Clunie, J. K. Baird, Interdiffusion Coefficient and Dynamic Viscosity for the Mixture 2,6-Lutidine Water near the Lower Consolute Point. *Phys. Chem. Liquids* **37**, 357–371 (1999). [doi:10.1080/00319109908031441](https://doi.org/10.1080/00319109908031441)
36. I. Buttinoni, G. Volpe, F. Kümmel, G. Volpe, C. Bechinger, Active Brownian motion tunable by light. *J. Phys. Condens. Matter* **24**, 284129 (2012). [doi:10.1088/0953-8984/24/28/284129](https://doi.org/10.1088/0953-8984/24/28/284129) [Medline](#)
37. C. Lozano, B. Ten Hagen, H. Löwen, C. Bechinger, Phototaxis of synthetic microswimmers in optical landscapes. *Nat. Commun.* **7**, 12828 (2016). [doi:10.1038/ncomms12828](https://doi.org/10.1038/ncomms12828) [Medline](#)
38. S. Das, A. Garg, A. I. Campbell, J. Howse, A. Sen, D. Velegol, R. Golestanian, S. J. Ebbens, Boundaries can steer active Janus spheres. *Nat. Commun.* **6**, 8999 (2015). [doi:10.1038/ncomms9999](https://doi.org/10.1038/ncomms9999) [Medline](#)
39. C. Bechinger, R. Di Leonardo, H. Löwen, C. Reichhardt, G. Volpe, G. Volpe, Active Particles in Complex and Crowded Environments. *Rev. Mod. Phys.* **88**, 045006 (2016). [doi:10.1103/RevModPhys.88.045006](https://doi.org/10.1103/RevModPhys.88.045006)
40. K. Martens, L. Angelani, R. Di Leonardo, L. Bocquet, Probability distributions for the run-and-tumble bacterial dynamics: An analogy to the Lorentz model. *Eur. Phys. J. E* **35**, 84 (2012). [doi:10.1140/epje/i2012-12084-y](https://doi.org/10.1140/epje/i2012-12084-y) [Medline](#)

41. A. P. Bregulla, H. Yang, F. Cichos, Stochastic localization of microswimmers by photon nudging. *ACS Nano* **8**, 6542–6550 (2014). [doi:10.1021/nn501568e](https://doi.org/10.1021/nn501568e) [Medline](#)
42. U. Khadka, V. Holubec, H. Yang, F. Cichos, Active particles bound by information flows. *Nat. Commun.* **9**, 3864 (2018). [doi:10.1038/s41467-018-06445-1](https://doi.org/10.1038/s41467-018-06445-1) [Medline](#)
43. G. Volpe, S. Gigan, G. Volpe, Simulation of the active Brownian motion of a microswimmer. *Am. J. Phys.* **82**, 659–664 (2014). [doi:10.1119/1.4870398](https://doi.org/10.1119/1.4870398)
44. L. P. Dadhichi, R. Chajwa, A. Maitra, S. Ramaswamy, Asymmetric exchange in flocks. arXiv [1605.00981](https://arxiv.org/abs/1605.00981) [cond-mat.stat-mech] (14 May 2016).
45. A. Cavagna, I. Giardina, A. Jelic, S. Melillo, L. Parisi, E. Silvestri, M. Viale, Nonsymmetric Interactions Trigger Collective Swings in Globally Ordered Systems. *Phys. Rev. Lett.* **118**, 138003 (2017). [doi:10.1103/PhysRevLett.118.138003](https://doi.org/10.1103/PhysRevLett.118.138003) [Medline](#)